AGU PUBLICATIONS

Geophysical Research Letters

RESEARCH LETTER
10.1002/2016GL069034

Special Section:
First results from NASA's Magnetospheric Multiscale (MMS) Mission

Kinetic signatures of the region surrounding the *X* line in asymmetric (magnetopause) reconnection

M. A. Shay[1], T. D. Phan[2], C. C. Haggerty[1], M. Fujimoto[3], J. F. Drake[4], K. Malakit[5], P. A. Cassak[6], and M. Swisdak[4]

[1]Bartol Research Institute, Department of Physics and Astronomy, University of Delaware, Newark, Delaware, USA, [2]Space Sciences Laboratory, University of California, Berkeley, California, USA, [3]ISAS, Kanagawa, Japan, [4]Institute for Research in Electronics and Applied Physics, University of Maryland, College Park, Maryland, USA, [5]Department of Physics, Mahidol University, Bangkok, Thailand, [6]Department of Physics and Astronomy, West Virginia University, Morgantown, West Virginia, USA

Key Points:
- Where the sunward normal electric field overlaps the magnetic field reversal (the "shoulder") is a signature of electron diffusion region
- Signatures in the regions upstream of the *X* line establish context to find the diffusion region
- Cusp-like motion of magnetosheath electrons associated with electron acceleration produce crescent-shaped particle distributions

Correspondence to:
M. A. Shay,
SHAY@UDEL.EDU

Citation:
Shay, M. A., T. D. Phan, C. C. Haggerty, M. Fujimoto, J. F. Drake, K. Malakit, P. A. Cassak, and M. Swisdak (2016), Kinetic signatures of the region surrounding the *X* line in asymmetric (magnetopause) reconnection, *Geophys. Res. Lett.*, *43*, 4145–4154, doi:10.1002/2016GL069034.

Received 9 MAR 2016
Accepted 20 APR 2016
Accepted article online 21 APR 2016
Published online 14 MAY 2016

Abstract Kinetic particle-in-cell simulations are used to identify signatures of the electron diffusion region (EDR) and its surroundings during asymmetric magnetic reconnection. A "shoulder" in the sunward pointing normal electric field ($E_N > 0$) at the reconnection magnetic field reversal is a good indicator of the EDR and is caused by magnetosheath electron meandering orbits in the vicinity of the *X* line. Earthward of the *X* line, electrons accelerated by E_N form strong currents and crescent-shaped distribution functions in the plane perpendicular to *B*. Just downstream of the *X* line, parallel electric fields create field-aligned crescent electron distribution functions. In the immediate upstream magnetosheath, magnetic field strength, plasma density, and perpendicular electron temperatures are lower than the asymptotic state. In the magnetosphere inflow region, magnetosheath ions intrude resulting in an Earthward pointing electric field and parallel heating of magnetospheric particles. Many of the above properties persist with a guide field of at least unity.

1. Introduction

Magnetic reconnection occurs in a small diffusion region around the *X* line but its consequences are large scale. Understanding kinetic processes in the diffusion regions for both symmetric (magnetotail-like) and asymmetric (magnetopause-like) reconnection is the primary objective of the current Magnetospheric Multiscale (MMS) mission. In the context of this paper, we define the electron diffusion region (EDR) to be the electron-scale region surrounding the *X* line in which magnetic connectivity is ultimately broken. Note that this definition is fundamentally nonlocal in nature.

Diffusion regions are minuscule so their detections by spacecraft are rare. A challenge for spacecraft observations is the identification of the diffusion region in data. There are different approaches to determine whether or not a spacecraft has encountered the diffusion region. One approach is to identify the diffusion region based on theoretically expected kinetic signatures of diffusion region: enhanced dissipation [e.g., *Zenitani et al.*, 2011]; nongyrotropic particle behavior [e.g., *Scudder and Daughton*, 2008; *Aunai et al.*, 2013; *Swisdak*, 2016]; or electron distribution functions [e.g., *Chen et al.*, 2008; *Ng et al.*, 2011]. While this approach is required to reveal diffusion region processes, some of the kinetic signatures are difficult to measure accurately in experiments. Furthermore, some signatures also exist downstream of the diffusion region and along the separatrices.

An alternative and complementary approach, taken in the present paper, is to identify diffusion region candidates by a combination of large-scale context, e.g., the properties of the region surrounding the ion and electron diffusion regions, and simple to measure signatures of the electron diffusion region itself. Such a scheme provides crucial consistency checks for the interpretation of diffusion region encounters based on observed kinetic signatures.

This paper addresses ways to recognize proximity to the diffusion region at the magnetopause where reconnection involves asymmetric inflow conditions. We focus on the case of antiparallel asymmetric reconnection (i.e., no guide field), but many of the signatures described are also present in guide field reconnection.

2. Simulations

We perform a particle-in-cell (PIC) simulation [*Zeiler et al.*, 2002] of asymmetric magnetic reconnection with no guide field. Magnetic field strengths and particle number densities are normalized to B_0 and n_0, respectively.

Lengths are normalized to the ion inertial length $d_{i0} = c/\omega_{pi0}$ at the reference density n_0, time to the ion cyclotron time $(\Omega_{ci0})^{-1} = m_i c/(e\, B_0)$, and velocities to the Alfven speed $c_{A0} = d_{i0} / \Omega_{ci0}$. Electric fields, temperatures, and energies are normalized to $E_0 = c_{A0}B_0/c$, $T_0 = m_i {c_{A0}}^2$, and $\varepsilon_0 = m_i\, {c_{A0}}^2$, respectively.

The simulations are 2½ dimensional and performed in the $L \times N$ plane of the *LMN* current sheet coordinate system, with the *L* being the reconnection outflow direction, *N* being the inflow direction, and *M* along the *X* line direction. The simulation domain size is 102.4 $d_i \times 51.2\ d_i$ with 2048×1024 grid cells, 50 particles per grid cell, $c/c_{A0} = 15$ ($\Omega_{ce0}/\omega_{pi0} = 1/3$), and $m_i/m_e = 25$. The initial conditions are an asymmetric double current sheet [*Malakit et al.*, 2010]. The simulation uses magnetosheath to magnetosphere density and magnetic field ratios of 10 and ½, respectively. $T_i/T_e = 2$ with $T_i = 1.33$ in the magnetosheath and 3.33 in the magnetosphere. A small magnetic perturbation is used to initiate reconnection. The simulation is evolved until reconnection reaches a steady state, and then for analysis purposes during this steady period the simulation data are time averaged over one ion cyclotron time $(\Omega_{ci0})^{-1}$. The parameters above are typical for the magnetopause, except c/c_{A0} and m_i/m_e, which are required to be unrealistic to keep the simulation size manageable since both the electron inertial length and the debye length must be resolved.

3. Electron Diffusion Region Signatures: Normal Electric Field Shoulder

Figure 1 shows simulation results in the *L*-*N* plane: magnetic and electric fields, electron and ion flows, current, density, temperatures, and different measures of the violation of the ion and electron frozen-in conditions. The solid contours are magnetic field lines and the dotted line is the midplane where $B_L = 0$. Electron diffusion regions should exhibit a number of properties such as (1) the violation of the electron frozen-in condition, (2) nongyrotropic electron distributions [e.g., *Scudder and Daughton*, 2008; *Aunai et al.*, 2013; *Scudder et al.*, 2015; *Swisdak*, 2016], and (3) enhanced dissipation [*Zenitani et al.*, 2011]. However, the violation of the frozen-in condition and nongyrotropic distributions in themselves do not uniquely define the electron diffusion region at the *X* line. In Figures 1m–1p are shown 2-D plots of $\mathbf{E} + \mathbf{V} \times \mathbf{B}$ for both the ions and electrons, along the *N* and *M* directions. In the *N* direction (Figures 1m–1n), both the electrons and ions show large values near the magnetospheric separatrices [*Mozer and Pritchett*, 2009]. In the *M* direction (Figures 1o–1p), although $\mathbf{E} + \mathbf{V} \times \mathbf{B}$ peaks close to the *X* line, it has significant value throughout the exhaust, even for the electrons.

A measure of nongyrotropy D_{ng} [*Aunai et al.*, 2013, Equation (2)] as shown in Figure 1q, is also not localized close to the *X* line. There is a large nongyrotropy near the magnetospheric separatrices (see also *Scudder et al.* [2012]) colocated with the strong E_N and weaker nongyrotropy on the magnetosheath separatrices. Such strong and long-lived nongyrotropy created by perpendicular electric fields has been demonstrated in kinetic PIC simulations of both antiparallel and component symmetric reconnection [*Scudder and Daughton*, 2008]. A frame independent dissipation measure $D_e = \boldsymbol{J} \cdot (\boldsymbol{E} + \boldsymbol{V}_e \times \boldsymbol{B}) - (n_i - n_e)(\boldsymbol{V}_e \cdot \boldsymbol{E})$ [*Zenitani et al.*, 2011] is strongly peaked very close to the *X* line in Figure 1r and is therefore a good parameter with which to identify the electron diffusion region, although D_e is slightly enhanced along the separatrices as well. Figures 1s and 1t show the nonnegligible terms of D_e: $E_{\parallel} J_{\parallel}$ and $\boldsymbol{J}_{\perp} \cdot (\boldsymbol{E}_{\perp} + \boldsymbol{V}_e \times \boldsymbol{B})$. Care must be taken when decomposing $\boldsymbol{J} \cdot \boldsymbol{E}$ into perpendicular and parallel terms, as in this case the large positive $E_{\parallel} J_{\parallel}$ near the *X* line is mostly canceled by the negative perpendicular term such that $\boldsymbol{J} \cdot \boldsymbol{E}$ is nearly zero in this region.

Our simulation reveals a simple to measure indicator of the electron diffusion in the form of a region of overlap between the sunward pointing normal electric field ($E_N > 0$) and the field reversal region $B_L = 0$. Below we denote this as the "overlap" or "shoulder" region. Note that E_N is the largest component of the electric field at the magnetopause [*Vaivads et al.*, 2004; *Pritchett*, 2008; *Tanaka et al.*, 2008]. Figures 2a–2j show 1-D profiles of various quantities along *N* through the *X* line. The strong E_N has a visible shoulder and is >0 at the midplane, which is the *X* line in this cut.

While $E_N > 0$ occurs all along the magnetospheric separatrix, extending long distances downstream of the *X* line, $E_N > 0$ only touches the midplane close to the *X* line (within 2.75 d_i along the outflow direction) and it exhibits a shoulder that is not seen away from the EDR. In Figures 3b and 3c are shown cuts of E_N at 1.75 d_i and 2.75 d_i (8.75 and 13.75 d_e) downstream of the *X* line. E_N is now displaced toward the magnetosphere side of the reversal region and by 2.75 d_i downstream no longer overlaps with $B_L = 0$. From Figures 1c, 1q, and 1r, the overlap/shoulder region coincides with the region of enhanced dissipation

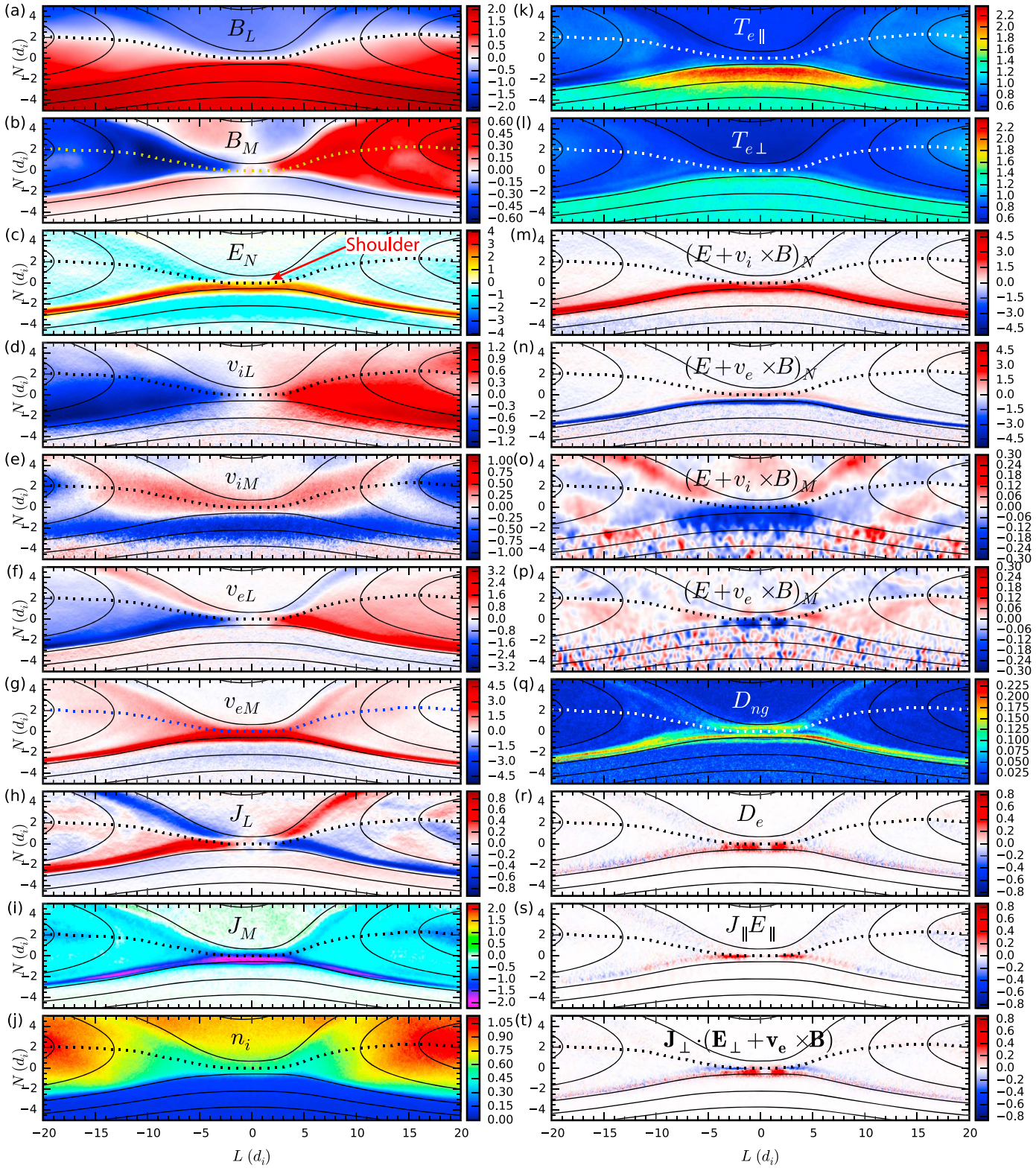

Figure 1. Simulation results in the *LN* plane. Quantities plotted denoted as text in each frame. D_{ng} is a nongyrotropy measure [*Aunai et al.*, 2013] and D_e is a dissipation measure [*Zenitani et al.*, 2011]. Solid black contours are magnetic field lines and dotted lines show the midplane (defined where $B_L = 0$).

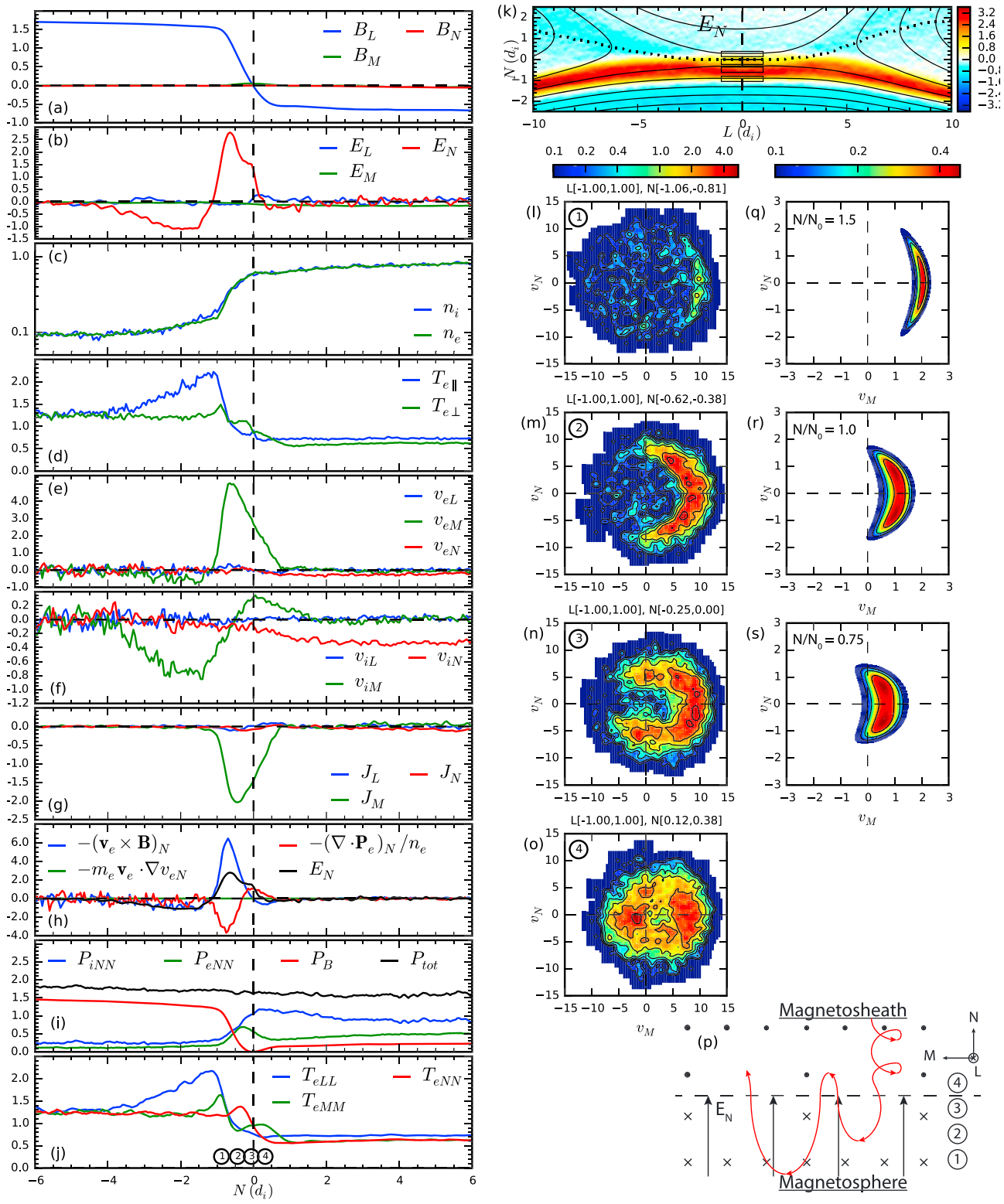

Figure 2. (a–j) One-dimensional spatial profiles along *N*, on the dashed line through the *X* line shown in the 2-D image in Figure 2k. (k) E_N, vertical dashed line is the location of 1-D cuts, dotted line is the midplane, rectangles denote locations of distribution functions. (l–o) Electron distribution functions in (V_M,V_N) plane. Distributions are integrated between $V_e = \pm 3$ (in electron bulk flow frame) along the third velocity direction V_L. Spatial domain sampled to create distributions shown in the title of each panel. (p) Schematic of magnetosheath electron motion in the vicinity of *X* line. (q–s) Distribution functions predicted from electron motion in linear ramp model of E_N and B_L. In Figure 2p, the corresponding positions of the phase space densities (Figures 2l–2o) and temperatures (Figure 2j) are denoted by the circled numbers 1–4.

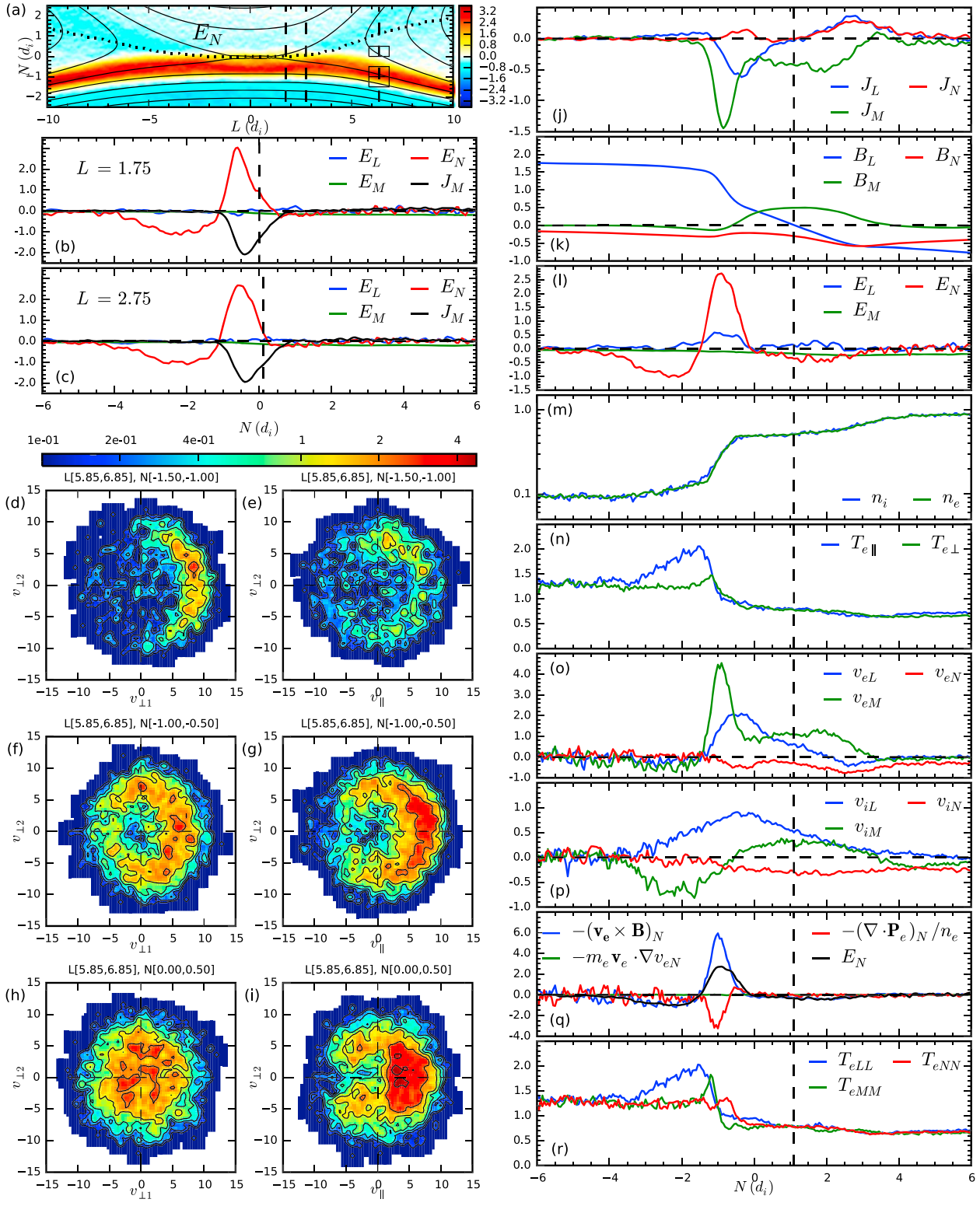

Figure 3. (a) E_N, vertical dashed line is the location of 1-D cuts, dotted line is the midplane, rectangles denote locations of distribution functions, (b, c) 1-D spatial profiles of E and J_M at 1.75 and 2.75 d_i downstream of X line. (d–i) Electron distribution functions in ($v_{\perp 1}$, $v_{\perp 2}$) and ($v_{\parallel}$, $v_{\perp 2}$) planes, integrated between $v = \pm 3$ along the third velocity direction (in electron bulk flow frame); $\mathbf{v}_{\perp 1}$ along $\mathbf{E}\times\mathbf{B}$ direction, and $\mathbf{v}_{\perp 2}$ along $\mathbf{B}\times(\mathbf{E}\times\mathbf{B})$. (j–r) One-dimensional spatial profiles along N taken 6.35 d_i downstream of X line. Vertical dashed line is the location of the midplane.

measure D_e and where the electrons are nongyrotropic, suggesting that this is a good indicator of the electron diffusion region. Indeed, it will be shown in the following paragraphs that the physics ultimately creating the shoulder is intimately linked to the electron kinetic physics associated with the electron diffusion region.

We now examine the kinetic behavior of the electrons in the region in the vicinity of the *X* line. The stagnation point of the electron flow occurs on the magnetospheric side of the *X* line [*Cassak and Shay*, 2007] and marks the transition between magnetosheath and magnetosphere plasma. Here there are strong gradients in density and electron temperature, as well as a peak in V_{eM} (Figures 2c–2e). Examination of the *N* component of Ohm's law reveals that the physics of the overlap/shoulder region is fundamentally different from the rest of the strong E_N region (that extends along the separatrices). The typical strong E_N is characterized by a large $(\mathbf{V}_e \times \mathbf{B})_N$ which is partially offset by a $(\nabla \cdot \mathbf{P}_e)_N$ of the opposite sign in Figures 2h and 3q. In the shoulder region in Figure 2h, however, $(\mathbf{V}_e \times \mathbf{B})_N$ becomes small and the electron pressure term changes sign, creating the shoulder on E_N at the *X* line.

The electron pressure gradient along *N* in this region is due to variation in P_{eNN} (Figure 2i). Approaching from the magnetospheric side, the magnetic pressure drops precipitously and is offset primarily by the increased pressure of the magnetosheath plasma. The same behavior is seen far downstream of the *X* line. However, in the shoulder region, the electron pressure gradient is also produced by a gradient of T_{eNN}, as shown in Figure 2j; quite striking also is that the peak in T_{eNN} is straddled by two peaks of T_{eMM}.

This structuring of the electron diagonal pressure terms is due to the magnetosheath electron orbits associated with the sharp gradients in the EDR. In Figure 2p is a schematic in the *M*-*N* plane of the magnetosheath electron motion in the vicinity of the *X* line. Sheath electrons cross the *X* line, are accelerated by E_N and turned by the magnetosphere B_L into the *M* direction, and then return to the *X* line. The motion is very similar to the cusp-like motion of pickup ions in the solar wind. This cusp-like motion in E_N rather than the usual meandering motion at the *X* line is responsible for the crescent velocity distribution (Figures 2l–2n) seen in previous studies [*Hesse et al.*, 2014]; note that n_{sheath}/n_{sphere} is much larger than in previous studies, so the crescents in Figure 2 are much more distinct. Close to the *X* line in Figures 2m and 2n, a full crescent shape is created by sheath electrons flowing both toward and away from the *X* line along *N*, creating a peak in T_{eNN} in Figure 2j. Deeper into the magnetosphere (Figure 2l), electrons are accelerated to higher energy creating a crescent at higher velocities. The electrons counterstreaming along *M* relative to the magnetospheric population creates a strong peak in T_{eMM}. Note also that these crescent distribution functions straddle the location of the peak of V_{eM} and J_m. This strong current causes a large change in B_L necessary to balance the large pressure gradient in this region.

Sheath electrons that have reflected from the magnetosphere side cross the *X* line onto magnetosheath field lines (Figure 2p) and are accelerated in the *M* direction by the reconnection electric field E_M. The motion of these high-velocity sheath electrons relative to the newly incoming sheath electrons creates counterstreaming electron beams along the *M* direction in the shoulder region, as seen in Figure 2o and leads to a second peak of T_{eMM} associated with the shoulder (point 4 in Figure 2j). These counterstreaming beams are created by the proximity of the $B_L = 0$ region to the strong E_N region (the shoulder), which creates the electron meandering motion [*Horiuchi and Sato*, 1994] unique to the electron diffusion region very close to the *X* line. This shoulder of E_N, because it is associated with kinetic electron orbits, has a width (along the *N* direction) of around 2 d_e and is expected to have a width comparable to electron scales when observed in the magnetosphere.

Unlike the shoulder of E_N and the associated counterstreaming electron beams along *M*, the crescent-shaped electron distribution functions are not nearly as localized around the *X* line. Shown in Figures 3d–3i are distribution functions and 1-D profiles at 6.35 d_i downstream of the *X* line. As expected there is no overlap between $E_N > 0$ and $B_L = 0$ (Figure 3l), no secondary peak of T_{eMM} (Figure 3r), and no counterstreaming electron beams associated with meandering orbits (Figure 3h). However, the strong peak in T_{eMM} on the magnetosphere side of the reversal region and the gradient of T_{eNN} associated with the large E_N are still present in Figure 3r. The phase space density plots still reveal the crescent-shaped distribution functions, with the crescent becoming almost circular but nonuniform in Figure 3f. Associated with this is a "parallel outflow crescent" in ($V_{||}$, $V_{\perp 2}$) space (Figure 3g). Notably, the peak velocity of this

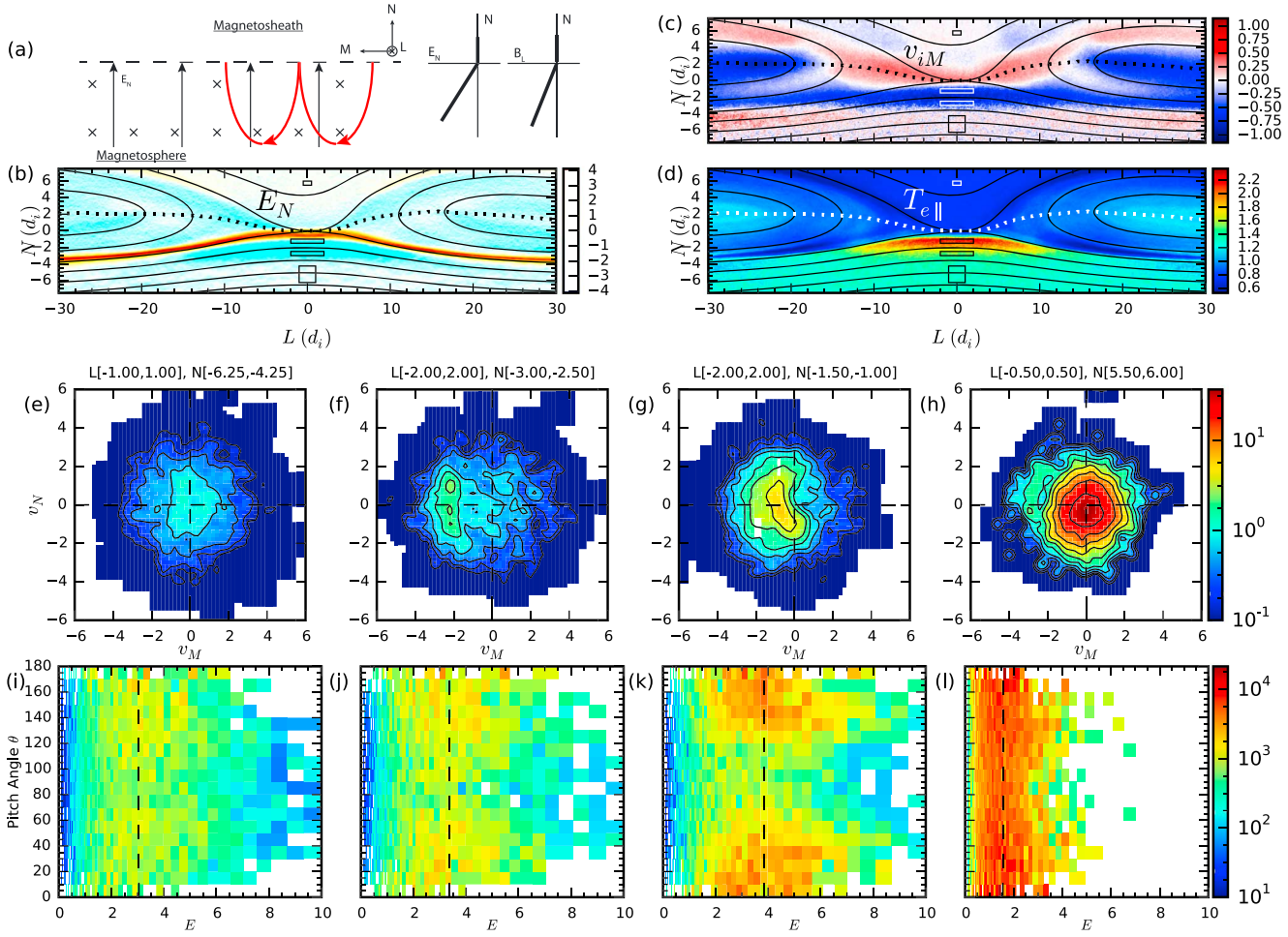

Figure 4. (a) Schematic of electron motion in linear ramp model with spatial variation of B_N and E_L. (b–d) Spatial profiles of E_N, V_{iM}, and $T_{e||}$. Dotted line is the midplane with boxes showing sampling locations used to create ion distribution functions and electron energy flux. (e–h) Ion distribution functions. Domain of sampling shown in the title of each frame; integrated between $v = \pm 0.6$ along the third direction (in ion bulk flow frame). (i–l) Electron energy flux dependence on energy and pitch angle θ. Domain sampling same as ion distribution function above each energy flux panel. Vertical dashed line is the electron core energy.

outflow crescent is the same as the crescent velocity around the *X* line. The streaming velocity results from a weak parallel electric field, which arises from the small value of B_N within the region of high E_N. The band of strong E_N downstream lies inside (magnetosheath side) of the separatrix, so the total potential drop along *B* downstream is the same as the potential drop along *N* at the *X* line. The parallel electron streaming velocity therefore matches the peak V_M at the *X* line. This outflow crescent starts to exist in the $\underline{E_N}$ shoulder only 1 $d_i = 5\ d_e$ downstream of the *X* line (not shown) and extends relatively far downstream (Figures 3e and 3g). These oppositely directed "parallel outflow crescents" are similar to those discovered by MMS around an *X* line [*Burch et al.*, 2016].

4. Theoretical Model for Crescent-Shaped Phase Space Density

This crescent distribution in Figures 2l–2n results from cusp-like orbits of electrons associated with the motion in the (*M*, *N*) plane controlled by $E_N(N)$ and $B_L(N)$ in the magnetosphere (*Burch et al.* [2016] and a similar model studied independently by *Bessho et al.* [2016]). In Figure 4a is a schematic showing both the simplified form of E_N and B_L and the electron particle motion. E_N and B_L are assumed to be zero on the magnetosheath side of the *X* line and then increase linearly with distance *N* into the magnetosphere so that $E_N = E_N' N$ and $B_L = B_L' N$ with the prime denoting a derivative with respect to *N*. For this situation the E × B velocity in the

M direction $V_{EB} = cE'_N/B'_L$ is independent of N. The reconnection electric field E_M has been neglected because it is more than 10 times smaller than E_N.

We focus on the motion in the (M, N) plane. The equations of motion can be integrated once to obtain two constants of motion, the canonical momentum P_M (V_M, N) in the M direction and the particle energy W in frame moving with a velocity V_{EB} in the M direction,

$$W = V_N^2 + (V_M - V_{EB})^2 = V_{N0}^2 + (V_{M0} - V_{EB})^2 \quad (1)$$

$$P_M = V_M - V_{EB}\frac{N^2}{N_0^2} = V_{M0}, \quad (2)$$

where $N_0 = \sqrt{-2\,V_{EB} m_e c/(eB'_L)}$ is the characteristic spatial scale length of the cusp-like orbits. Note that V_{EB} is positive while B'_L and E'_N are negative. V_{N0} and V_{M0} are the initial velocities of the electrons at $N = 0$. Eliminating V_M in (1) using (2), rearranging, we obtain

$$W_N = V_N^2 - 2(V_{EB} - V_{M0})\,V_{EB}\frac{N^2}{N_0^2} + V_{EB}^2\frac{N^4}{N_0^4} = V_{N0}^2 \quad (3)$$

The constancy of $W_N = W - (V_{M0} - V_{EB})^2$ implies that as a function of N, V_N first increases and then eventually goes to zero as the electrons are accelerated by E_N and then turned by B_L to return to $N = 0$. V_M reaches its maximum value at the maximum excursion of the electron in the N direction.

The electron distribution function f (V_M, V_N) in the region of finite E_N can be written in terms of the constants of motion W_N and P_M. We choose a form that produces a Maxwellian distribution of initial velocities V_{N0} and V_{M0}:

$$f(V_M,\ V_N) \propto e^{-P_M^2/v_{the}^2}\, e^{-W_N/v_{the}^2}\left[1 + \tanh\left(\frac{W_N}{v_{the}^2}\right)\right]/2, \quad (4)$$

where v_{the} is the electron thermal velocity at $N = 0$, V_{M0} in equation (2) is used in W_N and the tanh function forces W_N to be positive. The only free parameter is V_{EB}/v_{the}. For the simulations shown in Figure 2, $V_{EB} \approx 3.0$ and $N_0 \approx 0.4$. In Figures 2q–2s we show three modeled distribution functions at $N/N_0 = 0.75$, 1.0, and 1.5. The distributions are symmetric in V_N, corresponding to particles moving toward higher N and then returning. With increasing N there is a transition from a Maxwellian to a horseshoe distribution to a crescent with a peak at an increasing value of V_M but a narrower width along V_M.

5. Signatures of the Large-Scale Context Surrounding the *X* Line

The two inflow regions close to the X line exhibit distinct properties that can help identify the proximity to the X line and provide the context for satellite observations.

5.1. High-Density (Magnetosheath) Inflow Region

In typical magnetopause reconnection, the much weaker magnetic field of the inflowing magnetosheath plasma has a much larger inflow velocity (V_{iN}) compared with that on the magnetospheric side. This large inflow velocity leads to substantial bending of the magnetosheath field upstream of the X line (Figure 1) and results in an increased magnetic tension force away from the X line which leads to a reduction in total pressure relative to ambient magnetosheath conditions; both the reconnection magnetic field B_L and the plasma density n_i are decreased in this region of curved field lines. The spreading of the magnetic field also leads to a reduction in $T_{e\perp}$ (Figure 1l) and $T_{i\perp}$ (not shown).

5.2. Low-Density (Magnetospheric) Inflow Region

An earthward pointing "Larmor" electric field (cyan region in Figure 4b) exists in the magnetosphere inflow [*Malakit et al.*, 2013] as well as enhanced $T_{e\|}$ (Figure 4c) [*Egedal et al.*, 2011]; the electric field is responsible for generating the $T_{e\|}$ and both exist within ~15 d_i of the X line [*Malakit*, 2012]. We have explored other signatures in this region and found that the region is also characterized by the intrusion of the ion outflow (V_{iL}) jet (Figure 1d) and the out-of-plane V_{iM} (Figure 4c), while the electron flows (Figures 1f and 1g) are mostly confined to the magnetosheath side of the separatrix.

The distinct ion and electron flow behavior suggests that the penetration of the magnetosheath ions into the magnetosphere is due to an overshoot of the bulk motion of magnetosheath ions into the magnetosphere. This overshoot occurs because for asymmetric reconnection with large-density asymmetry, the stagnation point is located on the magnetospheric side of the reconnection layer [*Cassak and Shay*, 2007]. This overshoot from the finite ion Larmor gyroradius results in a net out-of-plane drift (i.e., V_M) of the magnetosheath ions as can be seen in the ion distributions (Figures 4e–4h). Associated with this negative V_M flow (and the positive B_L) is an earthward pointing normal electric field.

The lack of magnetosheath electron penetration into the magnetosphere is due to their smaller gyroradii. To achieve charge neutrality in the Larmor region where there is an excess of magnetosheath ions, the magnetospheric electrons are accelerated into the region by a parallel electric field, which results in a large parallel electron temperature increase in the region (Figure 4d). A key evidence for the magnetospheric electrons being responsible for the parallel temperature increase is shown in electron energy flux in Figures 4i–4l. The electron core energy is about 3.1 $m_i\, c_{A0}{}^2$ in the magnetosphere proper (Figure 4i) and 1.6 $m_i\, c_{A0}{}^2$ in the magnetosheath proper (Figure 4l). The electron distributions in the Larmor electric field region display strong field-aligned anisotropy and have a peak electron core energy of 3.85 $m_i\, c_{A0}{}^2$ in Figure 4k, higher than the core energy of magnetospheric electrons, which is consistent with them being heated magnetospheric electrons rather than heated magnetosheath electrons.

From the 1-D profiles in Figure 2a–2j, a spacecraft crossing normal to the magnetopause would detect no outflow ($V_L \sim 0$) and no out-of-plane Hall magnetic field, but would detect out-of-plane ion flow (V_M) in the magnetospheric inflow region, the associated Larmor ($E_n < 0$) electric field, and enhanced $T_{e\|}$. From Figures 3j–3r 6.35 d_i downstream of the X line, a spacecraft crossing this region would still measure the Larmor electric field and other associated signatures, but would also see a clear intrusion of V_{iL} into the magnetospheric inflow region (upstream the strong E_N).

6. Summary and Discussions

Using 2-D PIC simulations, we have examined signatures of the asymmetric reconnection electron diffusion region and its surroundings. We emphasize signatures that are relatively easy to measure experimentally. A simple and practical indicator of the electron diffusion region is the colocation of a sunward pointing E_N where $B_L = 0$ (called the "shoulder") as this signature coincides with the region of enhanced dissipation, non-gyrotropic electrons at midplane, and counterstreaming electron beams due to electron meandering orbits around the X line. This E_N signature is straightforward to measure experimentally because it is the largest component of the electric field at the magnetopause.

Crescent-shaped electron distribution functions in ($V_{\perp 1}$, $V_{\perp 2}$) plane and "parallel outflow crescents" in ($V_\|$, $V_{\perp 2}$) plane are associated with the strong E_N which occurs in asymmetric magnetic reconnection. While these signatures are not as localized as the E_N shoulder, spacecraft straddling the X line would observe oppositely directed "outflow crescents" [e.g., *Burch et al.*, 2016].

On a larger scale in the magnetospheric inflow region, a Larmor electric field is caused by the intrusion of magnetosheath ions into the magnetospheric inflow region and the resulting net out-of-plane flows of the penetrating magnetosheath ions. To preserve charge neutrality, magnetospheric electrons are drawn into the region, resulting in the enhancement of electron parallel temperature and an associated temperature anisotropy. The detection of the plasma and field signatures associated with the Larmor effect, including field-aligned temperature anisotropy, would imply that the spacecraft is within 15 ion skin depths of the X line.

On the magnetosheath side of the inflow region, the magnetic field magnitude, plasma density, and electron temperature are reduced compared to their upstream (asymptotic) values.

Acknowledgments
This research was supported by NSF grants AGS-1202330 and AGS-0953463; NASA grants NNX08A083G–MMS IDS, NNX14AC78G, NNX13AD72G, and NNX15AW58G; and the UDel NASA Space grant. Simulations and analysis were performed at NCAR-CISL and at NERSC. The data used are listed in the text, references, and are available by request.

References

Aunai, N., M. Hesse, and M. Kuznetsova (2013), Electron nongyrotropy in the context of collisionless magnetic reconnection, *Phys. Plasmas*, *20*, 092903, doi:10.1063/1.4820953.

Bessho, N., L.-J. Chen, and M. Hesse (2016), Electron distribution functions in the diffusion region of asymmetric magnetic reconnection, *Geophys. Res. Lett.*, *43*, 1828–1836, doi:10.1002/2016GL067886.

Burch, J. L., et al. (2016), Electron-scale measurements of magnetic reconnection in space, *Science*, doi:10.1126/science.aaf2939, in press.

Cassak, P. A., and M. A. Shay (2007), Scaling of asymmetric magnetic reconnection: General theory and collisional simulations, *Phys. Plasmas*, *14*, 102114, doi:10.1063/1.2795630.

Chen, L.-J., et al. (2008), Evidence of an extended electron current sheet and its neighboring magnetic island during magnetotail reconnection, *J. Geophys. Res.*, *113*, A12213, doi:10.1029/2008JA013385.

Egedal, J., A. Le, P. L. Pritchett, and W. Daughton (2011), Electron dynamics in two-dimensional asymmetric anti-parallel reconnection, *Phys. Plasmas*, *18*, 102901, doi:10.1063/1.3646316.

Hesse, M., N. Aunai, D. Sibeck, and J. Birn (2014), On the electron diffusion region in planar, asymmetric, systems, *Geophys. Res. Lett.*, *41*, 8673–8680, doi:10.1002/2014GL061586.

Horiuchi, R., and T. Sato (1994), Particle simulation study of driven magnetic reconnection in a collisionless plasma, *Phys. Plasmas*, *1*, 3587, doi:10.1063/1.870894.

Malakit, K. (2012), *Asymmetric Magnetic Reconnection: A Particle-in-Cell Study*, PhD thesis, Univ. of Delaware, Newark, Del.

Malakit, K., M. A. Shay, P. A. Cassak, and C. Bard (2010), Scaling of asymmetric magnetic reconnection: Kinetic particle-in-cell simulations, *J. Geophys. Res.*, *115*, A10223, doi:10.1029/2010JA015452.

Malakit, K., M. A. Shay, P. A. Cassak, and D. Ruffolo (2013), New electric field in asymmetric magnetic reconnection, *Phys. Rev. Lett.*, *111*, 135001, doi:10.1103/PhysRevLett.111.135001.

Mozer, F. S., and P. L. Pritchett (2009), Regions associated with electron physics in asymmetric magnetic field reconnection, *Geophys. Res. Lett.*, *36*, L07102, doi:10.1029/2009GL037463.

Ng, J., J. Egedal, A. Le, W. Daughton, and L.-J. Chen (2011), Kinetic structure of the electron diffusion region in antiparallel magnetic reconnection, *Phys. Rev. Lett.*, *106*, 065002, doi:10.1103/PhysRevLett.106.065002.

Pritchett, P. L. (2008), Collisionless magnetic reconnection in an asymmetric current sheet, *J. Geophys. Res.*, *113*, A06210, doi:10.1029/2007JA012930.

Scudder, J. D., R. D. Holdaway, W. S. Daughton, H. Karimabadi, V. Roytershteyn, C. T. Russell, and J. Y. Lopez (2012), First resolved observations of the demagnetized electron-diffusion region of an astrophysical magnetic-reconnection site, *Phys. Rev. Lett.*, *108*, 225005, doi:10.1103/PhysRevLett.108.225005.

Scudder, J. D., H. Karimabadi, W. Daughton, and V. Roytershteyn (2015), Frozen flux violation, electron demagnetization and magnetic reconnection, *Phys. Plasmas*, *22*, 101204, doi:10.1063/1.4932332.

Scudder, J., and W. Daughton (2008), "Illuminating" electron diffusion regions of collisionless magnetic reconnection using electron agyrotropy, *J. Geophys. Res.*, *113*, A06222, doi:10.1029/2008JA013035.

Swisdak, M. (2016), Quantifying gyrotropy in magnetic reconnection, *Geophys. Res. Lett.*, *43*, 43–49, doi:10.1002/2015GL066980.

Tanaka, K. G., et al. (2008), Effects on magnetic reconnection of a density asymmetry across the current sheet, *Ann. Geophys.*, *26*, 2471–2483, doi:10.5194/angeo-26-2471-2008.

Vaivads, A., Y. Khotyaintsev, M. Andre, A. Retino, S. C. Buchert, B. N. Rogers, P. Decreau, G. Paschmann, and T. D. Phan (2004), Structure of the magnetic reconnection diffusion region from four-spacecraft observations, *Phys. Rev. Lett.*, *93*, 105001, doi:10.1103/PhysRevLett.93.105001.

Zeiler, A., D. Biskamp, J. F. Drake, B. N. Rogers, M. A. Shay, and M. Scholer (2002), Three-dimensional particle simulations of collisionless magnetic reconnection, *J. Geophys. Res.*, *107*(A9), 1230, doi:10.1029/2001JA000287.

Zenitani, S., M. Hesse, A. Klimas, and M. Kuznetsova (2011), New measure of the dissipation region in collisionless magnetic reconnection, *Phys. Rev. Lett.*, *106*, 195003, doi:10.1103/PhysRevLett.106.195003.